Structural evidence for metal ion catalysis in the ribosome

Jason M. Hingey[1], Boris Rudolfs[1], Daniel B. Haack[1], Frank V. Murphy IV[2], Simpson Joseph[1] and Navtej Toor[1]*

[1]Department of Chemistry and Biochemistry, University of California, San Diego, La Jolla, CA

[2]Argonne National Laboratory, Advanced Photon Source, NE-CAT/Cornell University, Lemont, IL

*Correspondence should be addressed to N.T. (ntoor@ucsd.edu)

ABSTRACT:

Ribosomes synthesize proteins with an RNA-only active site across all kingdoms of life. Yet, despite decades of high-resolution ribosome structures, the precise catalytic mechanism has remained elusive. Here, we provide structural evidence for metal ion involvement in peptide bond formation, drawn from ribosome structures spanning bacteria, archaea, and eukaryotes. The metal ion resides in the active site, adjacent to a universally conserved stack of three base triples, reminiscent of the catalytic triplex in group II introns and the spliceosome, which catalyze pre-mRNA splicing. Metal-ion catalysis thus emerges as a fundamental unifying theme across the central dogma spanning protein synthesis, RNA splicing, and nucleic acid replication.

INTRODUCTION

The ribosome is essential to cellular life, carrying out the intricate task of translating genetic information into functional proteins through peptide bond formation. This process is at the core of the central dogma of molecular biology, in which information encoded in DNA is transcribed to RNA and then translated into proteins that perform nearly all cellular functions. The incredible conservation of the ribosome's structure and function across all kingdoms of life highlights its evolutionary importance. The first experimental evidence for the RNA-based catalytic function of the ribosome was based on extensive protein removal from ribosomes through proteinase K and SDS treatment while still resulting in retention of activity[1]. In contrast, activity was abolished by ribonuclease treatment[1]. This compelling biochemical evidence was later confirmed by high-resolution crystal structures revealing that its catalytic core, known as the peptidyl transferase center (PTC), is remarkably RNA-only, with no protein components directly involved in peptide bond formation[2]. These findings collectively established that the ribosome functions as a ribozyme, an RNA-based catalyst. Given the ribosome's essential role in sustaining life, understanding the precise catalytic mechanism of the PTC has been a long-standing goal in molecular biology.

The structural elucidation of the ribosome has been one of the great achievements in biology, yielding atomic-resolution insights into its architecture through X-ray crystallography and, more recently, cryo-electron microscopy (cryo-EM). Over the past two decades, numerous high-resolution ribosome structures from various species have revealed detailed views of its active site, RNA folding, and the positioning of tRNAs and mRNA during translation[2-6]. These structures have illustrated substrate binding and provided snapshots of the catalytic steps, yet we still lack a clear understanding of how the PTC catalyzes peptide bond formation with such

efficiency. This has led to various hypotheses suggesting that the ribosome may utilize alternative strategies, such as substrate positioning (entropic catalysis)[7], transition state stabilization through RNA interactions[8], contributions from acid-base catalysis by RNA[9,10], or involvement of solvent molecules in proton transfer[11,12]. However, there is no clear direct structural evidence to clarify how the chemical environment of the active site might stabilize transition states or lower activation barriers during peptide bond formation.

This gap in understanding is significant, as RNA-based catalysts generally exhibit lower catalytic efficiencies compared to protein enzymes[13], prompting questions about whether the ribosome might employ additional strategies to enhance its catalytic power. For example, while RNA alone can catalyze certain reactions, it often relies on metal ions for structural stability and catalytic enhancement. Metal ions are known to play crucial roles in other ribozymes, such as the group I[14,15] and group II introns[16,17], where they are essential for facilitating reactions by stabilizing transition states, activating nucleophiles, and providing electrostatic shielding[18]. However, until now, there was no structural evidence for the existence of a similar metal-ion-based mechanism that might play a role in peptide bond formation within the ribosome.

In this study, we determined the cryo-EM structure of the cytosolic 80S ribosome from *Chlamydomonas reinhardtii* (*C. reinhardtii*) at a global resolution of 2.7 Å, which indicated the presence of a metal ion within the PTC. We broadened our analysis to include published ribosome structures from many different species and found conservation of metal binding in the PTC across all kingdoms of life. Through the examination of eight structures from a range of archaeal, bacterial, and eukaryotic species, we identified a metal ion within the ribosomal active site. This metal ion is positioned alongside universally conserved rRNA residues, in close

association with a distinctive stack of three base triples. Here, we propose that the ribosome uses metal ion catalysis to power the formation of peptide bonds.

RESULTS

Presence of a metal ion in the peptidyl transferase center

To gain mechanistic insight into the PTC, we determined the cryo-EM structure of the cytosolic 80S ribosome from *Chlamydomonas reinhardtii*. This target was chosen because no high-resolution 80S cytosolic ribosome structures from photosynthetic organisms were available when we began, offering an opportunity to capture a novel snapshot of an actively translating ribosome. We purified native ribosomes (free of inhibitors or antibiotics) to preserve authentic catalytic states, and collected 4,032 movies on a Titan Krios. The resulting 3D reconstruction achieved an overall resolution of 2.7 Å (**Fig. 1A**). Focusing on the PTC, we looked for any electron density that might hint at reaction intermediates or catalytic cofactors.

Our initial analysis revealed a density peak in the PTC, consistent with a bound metal ion (**Fig. 1B**). This peak sits adjacent to the 2′-OH of C2063 (using *E. coli* numbering for rRNA residues) and lies in close proximity to the 2′-OH of A76 on the 3′ end of the peptidyl tRNA. Additionally, the metal ion is in the general vicinity of the N3 atom of A2451, a universally conserved nucleotide long studied for its role in catalysis[10,19]. Given its location bridging the P-site tRNA A76 (which carries the nascent peptide via an ester linkage at its 3′-OH) and rRNA residue C2063, we hypothesize that this metal ion could play a direct role in catalysis of peptide bond formation. Its proximity to the reacting groups suggests it might help activate the P-site carbonyl as an electrophile, stabilize transition states during the reaction, or stabilize the oxyanion of the tetrahedral intermediate. To test this hypothesis further, we surveyed prior

ribosome structures from the past 25 years to see if this metal site was a recurring, conserved feature.

Identification of metal ions in x-ray and cryo-EM maps

Identification of metal ions can be done in maps with a resolution better than 3 Å. Metal ions are typically prominent in crystal structures starting at this resolution. Metal ions are identified in crystal structures through an analysis of the coordination distance, coordination geometry, and peak strength. The biophysical properties of inner shell coordinated metal ions have been previously compiled from an analysis of crystal structures with a resolution better than 1.6 Å[20]. At this high resolution, the inner shell coordination distance for magnesium ranges from 2.1 to 2.3 Å. In structures that exhibit resolution poorer than 2.4 Å, the standard deviation for metal ion distances increases, potentially leading to a longer measured distance from the electron density map[20]. For example, the standard deviation increases from 0.2 to 0.5 Å as the resolution decreases from 1.6 to 2.2 Å[20]. Metal ion identity can also be inferred from coordination distance in the case of potassium, which has an inner shell distance ranging between 2.7 and 3.2 Å[20]. Coordination geometry with the surrounding protein/RNA ligands is also indicative of metal ion identity. Magnesium exhibits octahedral coordination geometry, whereas potassium has flexible geometry[20]. Finally, high peak strength with distinct spherical density in a crystallographic *Fo-Fc* omit map indicates that presence of an electron-rich metal ion.

Cryo-EM maps usually require higher resolution to resolve metal ions clearly. In our experience, cryo-EM structures need a local resolution of ~2.5 Å to visualize density for metal ions. In contrast to x-ray crystallography, it is relatively rare to see discrete metal ion density at a resolution of 3 Å in a cryo-EM map. Cryo-EM and x-ray crystallography differ fundamentally in their scattering mechanisms[21], which impacts their sensitivity to atomic charge. Cryo-EM

relies on electron scattering, which is influenced by the electrostatic potential (ESP) of the sample. This includes contributions from both the positively charged atomic nuclei and the electron cloud, making cryo-EM highly sensitive to the net charge of atoms. As a result, cations scatter strongly, while anions may produce weaker or even negative signals at low resolutions. In contrast, X-ray crystallography is based on photon scattering, which depends solely on electron density. This mechanism is charge-insensitive, meaning it cannot distinguish between ions like Mg^{2+} and neutral H_2O, as both scatter according to their total number of electrons. As a result, cryo-EM excels at detecting charge differences even at moderate resolutions (~2.5 Å), whereas X-ray crystallography requires high-resolution (better than 1.6 Å) maps and chemical context to differentiate between similar ions. Employing both cryo-EM and x-ray crystallography to identify a metal ion position is the most optimal situation.

Work done by Wang et al. (2018 and 2021) showed that the electrostatic potential maps of cryo-EM contain information beyond that found in x-ray crystallography to facilitate identification of metal ions[21,22]. Highly positively charged ions like magnesium exhibit an unusual effect in which the inner shell coordination between a magnesium ion and the polar N or O-containing ligand results in a delocalization of electrostatic potential that results in tubular density connecting these two atoms[22]. At short interaction distances (e.g., 2.0–2.2 Å), these peaks often merge with neighboring atom signals at low contour levels. This is a useful indicator of inner shell coordination and assists in metal ion identification. This arises because the strong positive charge is only partially offset by the partial negative charges of coordinating water molecules and base atoms. In contrast, phosphate group oxygens in the RNA backbone, which carry full negative charges, more effectively reduce the amplitudes of Mg^{2+} peaks, making these

peaks more discrete. This density characteristic is helpful in identifying multivalent cations like Mg^{2+} and is not seen for monovalent ions.

In our *C. reinhardtii* 80S map, the PTC region reaches the sub-2.7 Å local resolution range, enabling identification of the density described above as a likely Mg^{2+}. We strengthened this assignment by examining the shape of the density and its connectivity to nearby groups. The cryo-EM density appeared as a concentrated, tubular peak linking the putative Mg^{2+} to the coordinating 2′-OH ligand(s) (**Fig. 2A and 2B**). Indeed, at lower contour levels, we observed continuous tubular density connecting the metal to the O2′ of C2063, consistent with inner-sphere coordination. Such tubular connecting density is a hallmark of bound multivalent ions in cryo-EM maps, reflecting delocalized electrostatic potential between a multivalent cation and its ligands[21,22].

A conserved PTC metal ion across all kingdoms of life

Having established criteria for recognizing this PTC metal ion, we next asked whether previous high-quality ribosome structures showed evidence of a similar feature. We restricted our search to cryo-EM structures with local resolution ~2.5 Å in the PTC (to reliably detect a metal) and crystal structures resolved at high resolution, reasoning that if this metal were functionally important, it might appear in prior data even if not reported. Using our *C. reinhardtii* ribosome structure as a guide, we re-examined a diverse set of ribosome structures from bacteria, archaea, and eukaryotes for evidence of a metal ion in the PTC pocket defined by A76, C2063, and A2451. This survey yielded a clear result: we found the same PTC metal ion in multiple prior structures[23-27]. In total, we identified an unmodeled density consistent with a Mg^{2+} at this site in six additional cryo-EM reconstructions (**Fig. 2**), encompassing ribosomes from bacteria, plants, fungi, algae, and mammals. Notably, none of these deposited structures had modeled a

metal ion at this location in their original PDB files. In each case, the metal ion's position is directly at the site of catalysis: nestled where the peptide bond is formed, between the peptidyl-tRNA's ester linkage and universally conserved residues of the large subunit rRNA. The consistent presence of this density across evolutionarily distant species and in structures captured under different conditions underscores that this metal-binding site is a conserved feature of the ribosomal active site.

Closer inspection of the cryo-EM maps revealed a "ping-pong" behavior of this metal ion between two nearby coordinating oxygen ligands. In three of the structures, the metal is positioned closest to the 2′-OH of C2063 at the shortest distance of 2.09 Å, while in four structures the metal has the shortest distance of 2.05 Å to the 2′-OH of A76 from the P-site tRNA (**Table S1**). The metal moves ~1 Å in going from one hydroxyl to the other between these two different sets of structures. In most of these cases with a short distance, continuous density connects the metal to the O2′, indicating inner-sphere coordination to the ribose of these universally conserved nucleotides. These two states likely reflect the metal ion alternatively binding to either A76 or C2063. We infer that the metal can adopt at least two positions in the active site, effectively transferring ("ping-ponging") between A76 and C2063. Such a shift could correspond to different catalytic states of the ribosome, for instance before and after peptide bond formation (see Discussion). Importantly, in all instances the metal is stabilized by at least one inner-sphere contact to an RNA 2′-OH group and is in the vicinity of A2451. Based on the ~2.1 Å coordination distances observed, we conclude that this density corresponds to Mg^{2+} rather than a monovalent ion in each structure. These observations provide structural support for a Mg^{2+} bound in the ribosomal PTC in an analogous manner across species.

PTC metal ion in crystal structures of the ribosome

We next turned to X-ray crystal structures of the ribosome to see if the PTC metal is also evident in crystallographic electron density maps. We revisited an early high-resolution structure of the large ribosomal subunit from *Haloarcula marismortui* published in 2002[28]. In this 50S crystal structure of *H. marismortui* complexed with a P-site substrate analog (CCA-Phe-caproic acid–biotin) and the antibiotic sparsomycin, we observe strong positive difference density (7.6σ in a *Fo–Fc* omit map) corresponding to a Mg^{2+} at the site between the P-site substrate and A2451 (**Fig. 3**). The Mg^{2+} is coordinated to the 2′-OH of C2063 and also to the 2′-OH of the P-site tRNA A76 in an arrangement that is consistent with our cryo-EM observations, providing crystallographic evidence that independently corroborates the presence of the metal ion in the ribosomal active site. The consistency between cryo-EM and X-ray data underscores that this metal is not an artifact of one method or a specific sample, but rather a bona fide feature of the active site architecture.

Catalytic triplex in the PTC

In analyzing the RNA architecture around the metal ion, we found that the PTC contains a stack of three base triples that is universally conserved. These base triples form a rigid three-dimensional scaffold that cradles the metal ion. This base triple stack is present in all known structures of the ribosome. Such an arrangement of stacked base triples is relatively rare in RNA structures; however, it is common in ribozyme active sites utilizing a two-metal-ion mechanism[14,17,29-31]. Notably, this triple-helix motif bears a strong resemblance to the catalytic triplex described in group II introns and the spliceosome[17,29-31]. The group I intron is phylogenetically unrelated to the group II intron and the spliceosome, but it also contains three stacked base triples in the active site that form a binding pocket for two catalytic metal ions[14,15].

In group II intron ribozymes, the triple helix motif in the active site coordinates two Mg^{2+} ions and undergoes conformational rearrangements during splicing[16,32]. The ribosome's PTC triples appear to serve an analogous role: they position functional groups (such as the 2′-OH of A76 and the 2′-OH of C2063) in an orientation optimal for binding the metal ion and for interacting with substrates, providing an explanation for the strict conservation of nucleotide identities and the architectural arrangement within the triplex (**Fig. 4A** and **Movie S1**). A side-by-side comparison of the catalytic triplexes found in the ribosome, group II intron, spliceosome, and the group I intron shows structural homology (**Fig. 4B**). This parallel suggests an evolutionary convergence on using a triple-helix RNA scaffold to facilitate metal-ion catalysis in ribozymes. In summary, our structural results suggest that the ribosome's active site is organized to recruit and position at least one metal ion that may be involved in the catalysis of peptide bond formation, employing structural motifs and strategies strikingly similar to those found in self-splicing introns and other catalytic RNA systems.

DISCUSSION

Over two decades of research on peptide bond formation in the ribosome have greatly advanced our understanding of its catalytic efficiency, yet a unifying mechanism has remained elusive. Early on, the high-resolution structure of the large ribosomal subunit by Ban et al. (2000)[2] spurred numerous hypotheses to explain the ribosome's remarkable rate enhancement. Chief among these for many years was catalysis by approximation, the idea that the ribosome functions primarily as a positional catalyst by precisely aligning the A-site and P-site substrates to encourage bond formation[7]. While substrate alignment and strain relief (entropic catalysis) undoubtedly contribute to the ribosome's function, they alone have not fully accounted for the

observed reaction rate, especially given that RNA catalysts typically are far less efficient than protein enzymes[13]. Other proposed mechanisms included general acid-base catalysis by rRNA nucleotides (for instance, the suggestion that A2451 could shuttle protons due to its perturbed pK_a) and electrostatic stabilization of the transition state by the RNA environment[8,28]. However, integrating all biochemical and structural data into a single coherent model has proven difficult.

Our data and analysis indicates that the ribosome contains a metal adjacent to the 2′-OH of A76 from the P-site tRNA and the 2′-OH of the universally conserved rRNA C2063 of the large subunit rRNA. We hypothesize that this metal plays a catalytic role in peptide bond formation. This metal is optimally placed to stabilize the developing charges at the reaction center during the formation of the transition states and to interact with the 2′-OH of A76 from the peptidyl tRNA during the proton shuttling that has been suggested to produce the 3′-OH leaving group[33]. By coordinating to the ribose of A76, the metal ensures that the scissile carbonyl is held in an orientation conducive to reaction and that charge build-up is mitigated.

Our hypothesis of a metal-ion mechanism in the ribosome can be further evaluated against decades of biochemical data, much of which had been interpreted through other lenses. Two universally conserved residues in the PTC, A2451 (large subunit rRNA) and A76 (the terminal adenosine of tRNA), have been intensely studied for their contributions to catalysis. A2451 was originally proposed to be a general acid-base catalyst because it has an anomalously elevated pK_a (~7.6)[9,10]. However, mutating A2451 causes only a modest ~200 to 500-fold reduction in peptidyl transferase activity[9,34], which is difficult to reconcile with it being directly responsible for catalysis. In our structures, the N3 of A2451 is ~2.7 Å from the observed metal at its closest, depending on the state, and may interact transiently with this metal. A2451 might help position the metal (perhaps through transient coordination during the catalytic cycle) or modulate

its occupancy. This view explains why mutating A2451 impairs activity but does not abolish it, and why doubling of the magnesium concentration rescues much of the lost activity[34]. The participation of its 2′-OH in a proton shuttling network with the 2′-OH of the peptidyl tRNA A76 remains a viable mechanistic feature. In other words, the importance of the A2451 nucleobase can be rationalized by its influence on metal positioning and stability in the active site, which in turn affects catalysis.

The critical importance of the P-site tRNA 2′-OH group (A76) in catalysis has also been highlighted by several biochemical studies. Substitution of the 2′-OH with a deoxy group reduces peptide bond formation activity by $>10^6$-fold[35]. This million-fold rate reduction far exceeds the effects of any rRNA base mutation and underscores that the 2′-OH of A76 is absolutely essential for catalysis. Originally, this was puzzling: how could a single RNA hydroxyl on the substrate tRNA be so crucial? Our findings show that the 2′-OH serves as an inner-sphere ligand for the catalytic metal. When the hydroxyl is present, it binds and positions Mg^{2+} to assist catalysis; when this position is instead deoxygenated, the Mg^{2+} either cannot bind with the same affinity or is mispositioned, causing a catastrophic loss of catalytic rate. This phenomenon closely mirrors observations in the Tetrahymena group I ribozyme, where a specific 2′-OH in the substrate binding site (equivalent to a metal ligand) was found to be crucial: a 2′ deoxy substitution reduced the ribozyme's reaction rate by $\sim 10^5$ to 10^6-fold[36,37]. That result from the ribozyme world was one of the only prior indications hinting that the ribosome might also use a catalytic metal ion. Our work provides support for this hypothesis that the ribosome's reliance on the A76 2′-OH is because it anchors a catalytic Mg^{2+}. Thus, what was once viewed as the ribosome possibly needing an "RNA acid-base catalyst", and the puzzlement over why none of the rRNA mutations gave million-fold effects, can be reinterpreted: the RNA itself is not providing traditional

acid/base catalysis, but rather is providing ligands (like A76 2′-OH) to bind a metal ion that provides the catalysis. This idea was first proposed by Weinger et al. (2004) and to date, this remains the only direct reference to a possible catalytic metal ion in the ribosome literature[35]. Our work provides direct structural evidence for involvement of a metal ion in the active site of the ribosome.

In our analysis, we find that residue C2063 inner shell coordinates to the observed metal. Mutagenesis experiments involving C2063 and one of its interaction partners, A2450, revealed the disruption of this base pair led to impairment of translocation[38]. C2063 is also essential for ribosome function *in vivo*[39]. Given that the inner shell coordination with A76 places the metal in a closer position to the target substrate, while C2063 pulls this metal slightly away, we hypothesize that the movement to C2063 is required for the metal to "reset" before starting the next round of peptide bond formation. Therefore, we speculate that the ping-pong motion of this metal might be required for translocation of peptide substrates in the active site.

Additional support for a metal-based mechanism in the ribosome comes from outside the ribosome field as well. Remarkably, a Tetrahymena group I intron ribozyme, classically known for catalyzing self-splicing (via phosphodiester transfer), has been shown to catalyze a peptidyl ester hydrolysis reaction under artificial conditions[40]. In this study, Piccirilli and colleagues re-engineered the group I intron's active site to bind an N-formyl-methionyl-tRNA fragment, and demonstrated that this RNA enzyme can cleave the aminoacyl ester bond, essentially performing an aminoacyl-tRNA hydrolysis. This reaction is analogous to the reverse of peptide bond formation. They found that catalysis by the ribozyme required Mg^{2+} ions and intact catalytic core elements, showing that RNA can use metals to promote chemistry at a carbon center, not just at a phosphorus. This work greatly expanded the known catalytic repertoire of RNA and hinted that

the first aminoacyl-tRNA synthetase could have been an RNA. The fact that an unrelated ribozyme could be coaxed into handling an aminoacyl ester and needed magnesium to do so aligns with our finding that the most complex ribozyme of all, the ribosome, naturally utilizes magnesium to handle its aminoacyl ester substrates. The group I intron's aminoacyl esterase activity can be seen as a functional paralog of the ribosome's peptidyl transferase activity. Thus, what we observe and propose in the ribosome is not without precedent: it appears to be an RNA-world solution that has echoes in other systems.

It is also insightful to compare the ribosome's mechanism with that of purely protein enzymes that catalyze similar reactions. One example is carnosine dipeptidase 2 (CNDP2), a human enzyme that, in addition to being a dipeptidase, can condense small metabolites with amino acids (for instance, forming N-lactoyl-phenylalanine from lactate and phenylalanine) to form a peptide bond linkage[41]. More recently, it has been found to catalyze the condensation of beta-hydroxybutyrate (BHB) and phenylalanine to form BHB-Phe[42]. In both cases, an amino group is activated to attack a carboxyl group, leading to the formation of a peptide bond, much like the peptide bond formation that occurs in the ribosome's peptidyl transferase center. The active site of CNDP2 contains two Mn^{2+} ions that engage in a two-metal-ion mechanism, directly paralleling our hypothesis that the ribosome relies on divalent metal ions, particularly Mg^{2+}, for catalysis. Just as the ribosome positions substrates and harnesses Mg^{2+} to lower the activation barrier, CNDP2 uses Mn^{2+} to orient its substrates and stabilize the transition state. The existence of CNDP2 demonstrates that metal-ion catalysis can achieve peptide bond formation in a completely protein-based context, indicating that this is a fundamental biochemical strategy and not unique to RNA. The ribosome, as an RNA enzyme, appears to have pioneered the strategy

that protein enzymes like CNDP2 now use: deploying divalent metal ions to do the heavy lifting of neutralizing charges and activating nucleophiles during catalysis.

The classic two-metal-ion mechanism, first articulated for protein enzymes and ribozymes by Steitz and Steitz (1993)[43], is a recurring strategy in biology. This mechanism contributes to precise substrate positioning and transition-state (TS) stabilization in many enzymes involved in the processing or synthesis of nucleic acids. In DNA/RNA polymerases, for example, one Mg^{2+} (often called Metal A) coordinates the 3′-hydroxyl of the primer and helps deprotonate it, generating a strong nucleophile, while the second Mg^{2+} (Metal B) coordinates the incoming nucleotide's phosphate and stabilizes the developing negative charge as the transition state forms[44,45]. An almost identical principle operates in group I and II ribozymes that catalyze phosphodiester transfer: one metal ion activates the attacking 2′ or 3′-hydroxyl, and another stabilizes the leaving group and transition state[15,17,43]. Based on the structural homology of the catalytic triplexes we observe in the ribosome with those found in group I and II introns, we hypothesize that the ribosome may employ a two-metal ion mechanism similar to these other ribozymes. While our current data clearly identifies one metal ion in the PTC, a second metal ion may be present only transiently or under specific conditions not captured in our structures. This is analogous to what is seen in crystal structures of RNA polymerase in which one catalytic metal ion is constitutively bound in the active site, while the second metal transiently enters with the NTP substrate[46,47]. In the ribosome, this second metal could potentially play a role in nucleophile activation during peptide bond formation, complementing the role of the observed metal in stabilizing the transition state. Future structural and biochemical studies designed to capture different states of the catalytic cycle may reveal the position of this second metal ion. If

true, this would further validate the work by Steitz and Steitz (1993) stating that the two-metal-ion mechanism is ubiquitous in many different ribozymes.

Our findings not only provide new insights into ribosomal catalysis but also suggest a broader evolutionary conservation of metal-ion-based mechanisms across the central dogma of molecular biology. Our study provides a new lens through which to view the ribosome: not merely as a passive scaffold for bringing reactants together, but as an RNA enzyme that actively coordinates catalytic metal ions to achieve proficient peptide bond synthesis. This perspective unifies the ribosome's mechanism with those of polymerases and self-splicing ribozymes, suggesting that nature has repeatedly solved similar chemical challenges using the same fundamental toolkit of divalent metal ions. By demonstrating the structural presence and likely catalytic function of a metal in the ribosome, we hope to encourage researchers to revisit classical models of ribosome function and to design experiments that directly probe the role of this metal ion and the possible presence of an additional catalytic metal in the active site. Unraveling the full dynamics of the metal ion(s) during each elongation cycle will be an exciting challenge for the field, one that could reveal even more about how the ribosome has optimized its RNA active site for catalysis. Ultimately, this deeper understanding of ribosomal chemistry not only satisfies a fundamental scientific curiosity about the origin of biological catalysis but could also inform the development of novel antibiotics and shed light on how the translational apparatus evolved from simpler RNA-based precursors. The discovery of a metal ion in the ribosome PTC thus bridges a long-standing gap in molecular biology, connecting the mechanistic dots from the RNA World to modern protein synthesis, and highlighting once again the ingenious efficiency of life's molecular machines.

Taken together, these structural parallels support the notion that the conserved catalytic triplex observed in the ribosome, spliceosome, and group I/II ribozymes represents a primordial RNA enzyme motif dating back to the RNA World. This triple-helix tertiary interaction recurs at the active sites of all these molecular machines, where it positions reacting groups and coordinates catalytic metal ions. In group II introns (and similarly in the spliceosomal U6/U2 snRNA core), an AGC base-triad within this triplex binds two Mg^{2+} ions to facilitate a two-metal-ion mechanism for phosphoryl transfer. Likewise, a base triple sandwich stabilizes the catalytic core of a group I ribozyme. Even the peptidyl transferase center of the ribosome is buttressed by analogous base triples and metal ion coordination in the absence of proteins. We propose that this simple yet versatile motif constitutes the potential core of an ancestral replicase by aligning substrates and activating them through coordinated Mg^{2+} chemistry. This mechanism could have enabled template-directed RNA polymerization, thereby initiating the first self-perpetuating genetic cycles necessary for this critical step towards the emergence of life forms in the RNA World. It is tantalizing to speculate that the catalytic triplex found in the heart of the ribosome, spliceosome, and group I/II intron may be the engine that started life on earth.

MATERIALS & METHODS

C. reinhardtii ribosome purification

A 3-L culture of *C. reinhardtii* strain CC-400 was grown autotrophically in Sueoka's HS media[48] at 22 °C with 200 rpm orbital shaking, to a density of 1.8 x 10^7 cells/ml as determined by hemocytometer count. All subsequent steps were carried out at 4 °C. Cells were pelleted by centrifugation at 5,000 rcf for 10 minutes. The cell pellet was resuspended in 50 ml lysis buffer (150 mM NaCl, 60 mM KCl, 10 mM $MgCl_2$, 0.0085% n-dodecyl-β-D-maltoside, 100 mM

HEPES, pH 8.0) with Protease Inhibitor Cocktail VI (Millipore) added immediately prior to use. Cells were lysed using a probe sonicator for 2 minutes of total run time at 40% amplitude, using 10-second bursts and 60-second pause, and cell debris was cleared by centrifuging at 2,000 rcf for 30 min. The lysate was further cleared by ultracentrifugation at 40,000 rcf for 45 min. Bissulfosuccinimidyl suberate was then added to a working concentration of 1 mM in a 1-ml aliquot of the supernatant. The sample was loaded onto a 12-ml 10-50% sucrose gradient in lysis buffer, and ultracentrifuged at 115,000 rcf for 17 hours. The gradient was then fractionated into 1-ml aliquots, and 50 ul from the bottommost fraction of the gradient was passed through a mini Quick Spin RNA Column (Roche).

Single-particle cryo-EM sample preparation

3.5 ul of the purified ribosome sample was loaded onto a Quantifoil copper R2/2 300-mesh grid with 2-nm Holey Carbon film that had been glow discharged using a PELCO easiGlow (40 mBar, 15 mA for 30 sec). The grid was blotted for 5 sec with filter paper (Whatman No.1) and then immediately plunged into a liquid ethane/propane (37.5/62.5) mix using a manual plunger.

Single particle cryo-EM data collection and processing

4032 movies were collected on a Titan Krios microscope (Thermo Fisher) operating at 300 keV, equipped with a K3 Gatan direct electron detector, and with a magnification of 81,000x for a physical pixel size of 1.05 Angstroms and camera operating in super-resolution mode (0.524 Å/pixel). Movies were collected as 50 dose-fractionated frames for 7.3 s with a dose rate of 7.5 e^-/px/s, for a total dose of 50 $e^-/Å^2$, with a nominal defocus range of -1.0 to -2.5 microns.

Super resolution movies were imported into Relion 3.1[49,50] and motion corrected with a pixel binning of 2 to make the pixel size 1.05 Å/px, using Relion's internal version of

MotionCor2[51]. These 4032 exposures were then imported into cryoSPARC 4.1.2[52], and CTF corrected using cryoSPARC's Patch CTF. 780,255 particles were picked on 4,032 micrographs using Blob picker with a minimum particle diameter of 250 Å and a maximum particle diameter of 325 Å. 130 of these micrographs and corresponding 23,291 particles were manually removed based on poor CTF fit.

The cryo-workflow methods is described in **Fig. S1**. In brief, the 756,964 particles were extracted with a 144 pixel box (3.14 Å/px). Particles close to the edge of the micrograph were automatically discarded, and the remaining 595,520 particles were subjected to a single round of 2D classification. Particles from 2D classes that looked like the ribosome were selected for a 2-class ab initio model generation. The volumes generated here were then used for a single round of heterogenous classification. These particles were used for homogenous refinement, which was used to generate a set of 2D templates for cryoSPARC's template particle picker.

695,548 particles from template picker and the 164,511 particles from blob picker were extracted with a 180 pixel box (3.14 Å/px), and put through several rounds of 2D and heterogenous refinement for 3D classification. The remaining 345,502 particles were put through refinement, and re-extracted with a 432 pixel box (1.31 Å/px). In order to remove duplicate particles from the combined blob and template picking, particles with 3D alignment centers within 50 Å were removed. These particles were then extracted with an unbinned 540 pixel box (1.05 Å/px), and subjected to another round of duplicate removal. These 201,007 particles were then refined, and classified using cryoSPARC's 3D classification algorithm, using the default size of 10 classes. The class with no E-site tRNA was selected for non-uniform refinement. These 71,404 particles selected were refined to 2.73 Å after non-uniform refinement.

rRNA and protein sequences

Ribosomal RNA and protein sequences were retrieved by running corresponding sequences from the *N. tabacum* ribosome (based on those available in a published structure, PDB ID: 8B2L) through NCBI's BLAST[53] and restricting results to the organism *Chlamydomonas reinhardtii*. The sequence for eL39 could not be found via BLAST searches of the NCBI protein database, and was instead identified via a BLAST search of the UniParc archive within the UniProt database (https://www.uniprot.org/).

***C. reinhardtii* ribosome model building**

Modeling of the 80S ribosome of *C. reinhardtii* was performed by first using UCSF Chimera[54] to manually dock a model of the *S. cerevisiae* and *N. tabacum* 80S ribosomes (PDB IDs 6WOO and 8B2L, respectively) into the *C. reinhardtii* electron density map, followed by use of the "fit in map" tool, for ease of identification of rRNA sequence register and ribosomal protein locations. Modeling of rRNA was then performed in Coot[55] using the RCrane[56,57] plugin by removing the docked rRNA content after identifying the sequence register and then modeling into the empty density. The 3′CCA of the P-site tRNA was modeled into the density *de novo*. Ribosomal proteins were modeled in Coot by mutating the docked proteins and using real space refinement of small stretches (~5-20 amino acids) to precisely place each residue. The 60S and 40S subunits were modeled from two distinct maps that exhibited slightly higher resolution for the corresponding subunit compared to the 80S map, and additional local refinement maps produced in cryoSPARC were used to facilitate modeling at various regions around the periphery of the ribosome. Upon completion of model building, the 60S and 40S models were each fit into the density of the 80S map using the "fit in map" tool in Chimera. The interface between the subunits was examined in Coot, and real space refinement was used to perform several minor

adjustments along the interface to better fit the density of the 80S map and fix any potential steric clashes before merging the two subunits into a single model file. All software was compiled by SBGrid[58].

Statistical analysis

To calculate per-nucleotide all-atom RMSD values, models of the triplex from each structure indicated were superposed with the triplex from C. reinhardtii in COOT using LSQ superpose, and the superposed models were then opened in UCSF Chimera for analysis. Movie S1 was generated from the superposed models by using the Spin Movie function in UCSF Chimera. All map/model validation and statistics were done in PHENIX[59,60] (**Table S2**).

ACKNOWLEDGEMENTS: We would like to thank the Cal-Cryo Facility at UC Berkeley and Daniel Toso for assistance with data collection. This work was supported by National Institutes of Health grants R35GM141706 (N.T.) and R35GM141864 (S.J.).

AUTHOR CONTRIBUTIONS:

Conceptualization: JMH, BR, NT

Methodology: JMH, BR, DBH, FVM, SJ, NT

Investigation: JMH, BR, DBH, FVM, SJ, NT

Visualization: JMH, BR, DBH, FVM, SJ, NT

Supervision: SJ, NT

Writing—original draft: JMH, BR, DBH, SJ, NT

Writing—review & editing: JMH, BR, DBH, SJ, NT

COMPETING INTERESTS: None.

REFERENCES

1 Noller, H. F., Hoffarth, V. & Zimniak, L. Unusual resistance of peptidyl transferase to protein extraction procedures. *Science* **256**, 1416-1419 (1992). https://doi.org/10.1126/science.1604315

2 Ban, N., Nissen, P., Hansen, J., Moore, P. B. & Steitz, T. A. The complete atomic structure of the large ribosomal subunit at 2.4 A resolution. *Science* **289**, 905-920 (2000).

3 Korostelev, A., Trakhanov, S., Laurberg, M. & Noller, H. F. Crystal structure of a 70S ribosome-tRNA complex reveals functional interactions and rearrangements. *Cell* **126**, 1065-1077 (2006). https://doi.org/10.1016/j.cell.2006.08.032

4 Yusupov, M. M. *et al.* Crystal structure of the ribosome at 5.5 A resolution. *Science* **292**, 883-896 (2001). https://doi.org/10.1126/science.1060089

5 Selmer, M. *et al.* Structure of the 70S ribosome complexed with mRNA and tRNA. *Science* **313**, 1935-1942 (2006). https://doi.org/10.1126/science.1131127

6 Wimberly, B. T. *et al.* Structure of the 30S ribosomal subunit. *Nature* **407**, 327-339 (2000). https://doi.org/10.1038/35030006

7 Sievers, A., Beringer, M., Rodnina, M. V. & Wolfenden, R. The ribosome as an entropy trap. *Proc Natl Acad Sci U S A* **101**, 7897-7901 (2004). https://doi.org/10.1073/pnas.0402488101

8 Nissen, P., Hansen, J., Ban, N., Moore, P. B. & Steitz, T. A. The structural basis of ribosome activity in peptide bond synthesis. *Science* **289**, 920-930 (2000). https://doi.org/10.1126/science.289.5481.920

9 Katunin, V. I., Muth, G. W., Strobel, S. A., Wintermeyer, W. & Rodnina, M. V. Important contribution to catalysis of peptide bond formation by a single ionizing group within the ribosome. *Mol Cell* **10**, 339-346 (2002). https://doi.org/10.1016/s1097-2765(02)00566-x

10 Muth, G. W., Ortoleva-Donnelly, L. & Strobel, S. A. A single adenosine with a neutral pKa in the ribosomal peptidyl transferase center. *Science* **289**, 947-950 (2000). https://doi.org/10.1126/science.289.5481.947

11 Wallin, G. & Aqvist, J. The transition state for peptide bond formation reveals the ribosome as a water trap. *Proc Natl Acad Sci U S A* **107**, 1888-1893 (2010). https://doi.org/10.1073/pnas.0914192107

12 Polikanov, Y. S., Steitz, T. A. & Innis, C. A. A proton wire to couple aminoacyl-tRNA accommodation and peptide-bond formation on the ribosome. *Nat Struct Mol Biol* **21**, 787-793 (2014). https://doi.org/10.1038/nsmb.2871

13 Lilley, D. M. in *Philos Trans R Soc Lond B Biol Sci* Vol. 366 2910-2917 (2011).

14 Adams, P. L., Stahley, M. R., Kosek, A. B., Wang, J. & Strobel, S. A. Crystal structure of a self-splicing group I intron with both exons. *Nature* **430**, 45-50 (2004). https://doi.org/10.1038/nature02642

15 Stahley, M. R. & Strobel, S. A. Structural evidence for a two-metal-ion mechanism of group I intron splicing. *Science* **309**, 1587-1590 (2005). https://doi.org/10.1126/science.1114994

16 Robart, A. R., Chan, R. T., Peters, J. K., Rajashankar, K. R. & Toor, N. Crystal structure of a eukaryotic group II intron lariat. *Nature* **514**, 193-197 (2014). https://doi.org/10.1038/nature13790
17 Toor, N., Keating, K. S., Taylor, S. D. & Pyle, A. M. Crystal structure of a self-spliced group II intron. *Science* **320**, 77-82 (2008).
18 Lambowitz, A. M. & Zimmerly, S. Group II introns: mobile ribozymes that invade DNA. *Cold Spring Harb Perspect Biol* **3**, a003616 (2011). https://doi.org/10.1101/cshperspect.a003616
19 Lang, K., Erlacher, M., Wilson, D. N., Micura, R. & Polacek, N. The role of 23S ribosomal RNA residue A2451 in peptide bond synthesis revealed by atomic mutagenesis. *Chem Biol* **15**, 485-492 (2008). https://doi.org/10.1016/j.chembiol.2008.03.014
20 Harding, M. M. Geometry of metal-ligand interactions in proteins. *Acta Crystallogr D Biol Crystallogr* **57**, 401-411 (2001). https://doi.org/10.1107/s0907444900019168
21 Wang, J., Liu, Z., Frank, J. & Moore, P. B. Identification of ions in experimental electrostatic potential maps. *IUCrJ* **5**, 375-381 (2018). https://doi.org/10.1107/S2052252518006292
22 Wang, J., Natchiar, S. K., Moore, P. B. & Klaholz, B. P. Identification of Mg^{2+} ions next to nucleotides in cryo-EM maps using electrostatic potential maps. *Acta Crystallogr D Struct Biol* **77**, 534-539 (2021). https://doi.org/10.1107/S2059798321001893
23 Sehgal, E. *et al.* High-resolution reconstruction of a C. elegans ribosome sheds light on evolutionary dynamics and tissue specificity. *RNA* **30**, 1513-1528 (2024). https://doi.org/10.1261/rna.080103.124
24 Smirnova, J. *et al.* Structure of the actively translating plant 80S ribosome at 2.2 Å resolution. *Nat Plants* **9**, 987-1000 (2023). https://doi.org/10.1038/s41477-023-01407-y
25 Tesina, P. *et al.* Molecular mechanism of translational stalling by inhibitory codon combinations and poly(A) tracts. *EMBO J* **39**, e103365 (2020). https://doi.org/10.15252/embj.2019103365
26 Bhatt, P. R. *et al.* Structural basis of ribosomal frameshifting during translation of the SARS-CoV-2 RNA genome. *Science* **372**, 1306-1313 (2021). https://doi.org/10.1126/science.abf3546
27 Fromm, S. A. *et al.* The translating bacterial ribosome at 1.55 Å resolution generated by cryo-EM imaging services. *Nat Commun* **14**, 1095 (2023). https://doi.org/10.1038/s41467-023-36742-3
28 Hansen, J. L., Schmeing, T. M., Moore, P. B. & Steitz, T. A. Structural insights into peptide bond formation. *Proc Natl Acad Sci U S A* **99**, 11670-11675 (2002). https://doi.org/10.1073/pnas.172404099
29 Hang, J., Wan, R., Yan, C. & Shi, Y. Structural basis of pre-mRNA splicing. *Science* **349**, 1191-1198 (2015). https://doi.org/10.1126/science.aac8159
30 Galej, W. P. *et al.* Cryo-EM structure of the spliceosome immediately after branching. *Nature* **537**, 197-201 (2016). https://doi.org/10.1038/nature19316
31 Bertram, K. *et al.* Cryo-EM structure of a human spliceosome activated for step 2 of splicing. *Nature* **542**, 318-323 (2017). https://doi.org/10.1038/nature21079
32 Chan, R. T. *et al.* Structural basis for the second step of group II intron splicing. *Nat Commun* **9**, 4676 (2018). https://doi.org/10.1038/s41467-018-06678-0

33 Hiller, D. A., Singh, V., Zhong, M. & Strobel, S. A. A two-step chemical mechanism for ribosome-catalysed peptide bond formation. *Nature* **476**, 236-239 (2011). https://doi.org/10.1038/nature10248
34 Youngman, E. M., Brunelle, J. L., Kochaniak, A. B. & Green, R. The active site of the ribosome is composed of two layers of conserved nucleotides with distinct roles in peptide bond formation and peptide release. *Cell* **117**, 589-599 (2004). https://doi.org/10.1016/s0092-8674(04)00411-8
35 Weinger, J. S., Parnell, K. M., Dorner, S., Green, R. & Strobel, S. A. Substrate-assisted catalysis of peptide bond formation by the ribosome. *Nat Struct Mol Biol* **11**, 1101-1106 (2004). https://doi.org/10.1038/nsmb841
36 Bass, B. L. & Cech, T. R. Ribozyme inhibitors: deoxyguanosine and dideoxyguanosine are competitive inhibitors of self-splicing of the Tetrahymena ribosomal ribonucleic acid precursor. *Biochemistry* **25**, 4473-4477 (1986). https://doi.org/10.1021/bi00364a001
37 Moran, S., Kierzek, R. & Turner, D. H. Binding of guanosine and 3' splice site analogues to a group I ribozyme: interactions with functional groups of guanosine and with additional nucleotides. *Biochemistry* **32**, 5247-5256 (1993). https://doi.org/10.1021/bi00070a037
38 Chirkova, A. *et al.* The role of the universally conserved A2450-C2063 base pair in the ribosomal peptidyl transferase center. *Nucleic Acids Res* **38**, 4844-4855 (2010). https://doi.org/10.1093/nar/gkq213
39 Sato, N. S., Hirabayashi, N., Agmon, I., Yonath, A. & Suzuki, T. Comprehensive genetic selection revealed essential bases in the peptidyl-transferase center. *Proc Natl Acad Sci U S A* **103**, 15386-15391 (2006). https://doi.org/10.1073/pnas.0605970103
40 Piccirilli, J. A., McConnell, T. S., Zaug, A. J., Noller, H. F. & Cech, T. R. Aminoacyl esterase activity of the Tetrahymena ribozyme. *Science* **256**, 1420-1424 (1992). https://doi.org/10.1126/science.1604316
41 Jansen, R. S. *et al.* N-lactoyl-amino acids are ubiquitous metabolites that originate from CNDP2-mediated reverse proteolysis of lactate and amino acids. *Proc Natl Acad Sci U S A* **112**, 6601-6606 (2015). https://doi.org/10.1073/pnas.1424638112
42 Moya-Garzon, M. D. *et al.* A β-hydroxybutyrate shunt pathway generates anti-obesity ketone metabolites. *Cell* **188**, 175-186.e120 (2025). https://doi.org/10.1016/j.cell.2024.10.032
43 Steitz, T. A. & Steitz, J. A. A general two-metal-ion mechanism for catalytic RNA. *Proc Natl Acad Sci U S A* **90**, 6498-6502 (1993).
44 Freemont, P. S., Friedman, J. M., Beese, L. S., Sanderson, M. R. & Steitz, T. A. Cocrystal structure of an editing complex of Klenow fragment with DNA. *Proc Natl Acad Sci U S A* **85**, 8924-8928 (1988). https://doi.org/10.1073/pnas.85.23.8924
45 Beese, L. S. & Steitz, T. A. Structural basis for the 3'-5' exonuclease activity of Escherichia coli DNA polymerase I: a two metal ion mechanism. *EMBO J* **10**, 25-33 (1991). https://doi.org/10.1002/j.1460-2075.1991.tb07917.x
46 Wang, D., Bushnell, D. A., Westover, K. D., Kaplan, C. D. & Kornberg, R. D. Structural basis of transcription: role of the trigger loop in substrate specificity and catalysis. *Cell* **127**, 941-954 (2006). https://doi.org/10.1016/j.cell.2006.11.023
47 Vassylyev, D. G. *et al.* Structural basis for substrate loading in bacterial RNA polymerase. *Nature* **448**, 163-168 (2007). https://doi.org/10.1038/nature05931
48 Sueoka, N. Mitotic Replication Of Deoxyribonucleic Acid In Chlamydomonas Reinhardi. *Proc Natl Acad Sci U S A* **46**, 83-91 (1960). https://doi.org/10.1073/pnas.46.1.83

49 Kimanius, D., Forsberg, B. O., Scheres, S. & Lindahl, E. Accelerated cryo-EM structure determination with parallelisation using GPUs in RELION-2. *bioRxiv* (2016).
50 Scheres, S. H. RELION: implementation of a Bayesian approach to cryo-EM structure determination. *J Struct Biol* **180**, 519-530 (2012). https://doi.org/10.1016/j.jsb.2012.09.006
51 Zheng, S. Q. *et al.* MotionCor2: anisotropic correction of beam-induced motion for improved cryo-electron microscopy. *Nat Methods* **14**, 331-332 (2017). https://doi.org/10.1038/nmeth.4193
52 Punjani, A., Rubinstein, J. L., Fleet, D. J. & Brubaker, M. A. cryoSPARC: algorithms for rapid unsupervised cryo-EM structure determination. *Nat Methods* **14**, 290-296 (2017). https://doi.org/10.1038/nmeth.4169
53 Altschul, S. F., Gish, W., Miller, W., Myers, E. W. & Lipman, D. J. Basic local alignment search tool. *J Mol Biol* **215**, 403-410 (1990). https://doi.org/10.1016/S0022-2836(05)80360-2
54 Pettersen, E. F. *et al.* UCSF Chimera-a visualization system for exploratory research and analysis. *J Comput Chem* **25**, 1605-1612 (2004). https://doi.org/10.1002/jcc.20084
55 Emsley, P. & Cowtan, K. Coot: model-building tools for molecular graphics. *Acta Crystallogr D Biol Crystallogr* **60**, 2126-2132 (2004). https://doi.org/10.1107/s0907444904019158
56 Keating, K. S. & Pyle, A. M. Semiautomated model building for RNA crystallography using a directed rotameric approach. *Proc Natl Acad Sci U S A* **107**, 8177-8182 (2010). https://doi.org/0911888107
57 Keating, K. S. & Pyle, A. M. RCrane: semi-automated RNA model building. A*cta Crystallogr D Biol Crystallogr* 6**8,** 985-995 (2012). https://doi.org/10.1107/s0907444912018549
58 Morin, A. *et al.* Collaboration gets the most out of software. E*life* 2**,** e01456 (2013). https://doi.org/10.7554/eLife.01456
59 Adams, P. D. *et al.* PHENIX: a comprehensive Python-based system for macromolecular structure solution. A*cta Crystallogr D Biol Crystallogr* 6**6,** 213-221 (2010).
60 Afonine, P. V. *et al.* Real-space refinement in PHENIX for cryo-EM and crystallography. A*cta Crystallogr D Struct Biol* 7**4,** 531-544 (2018). https://doi.org/10.1107/S2059798318006551

FIGURE LEGENDS

Figure 1. Structure of the *Chlamydomonas reinhardtii* cytosolic ribosome (A) Overview of electrostatic potential map of the *Chlamydomonas reinhardtii* 80S ribosome from cryo-electron microscopy. RNA content is shown in dark blue and dark yellow. Protein content is shown in light blue and light yellow. (B) The peptidyl transferase center of the *C. reinhardtii* 80S ribosome, shown with and without the cryo-EM density. Density corresponding to a metal ion extends from the 2′-OH of C2063 (using conventional *E. coli* numbering). The metal ion is modeled into the density as an orange sphere.

Figure 2. Comparison of the metal ion binding in the PTC. (A) Cryo-EM maps showing connective density between the metal ion and the 2′-OH of A76 from the P-site tRNA in various structures. (B) Cryo-EM maps showing connective density between the metal ion and the 2′-OH of C2063 from the P-site tRNA in various structures. (C) An overlay of the PDBs from panels A and B reveals the high degree of conservation in the architecture of this region.

Figure 3. Metal ion binding site in a crystal structure of the archaeal 50S ribosome in complex with a substrate analog. (A) Crystallographic *Fo-Fc* map contoured at 3σ from PDB deposition 1M90, showing strong (7.6σ), spherical positive density consistent with a metal ion. (B) Crystallographic *2Fo-Fc* map contoured at 1σ, after refining PDB deposition 1M90 with Mg^{2+} modeled into the electron density.

Figure 4. Structural homology in the catalytic triplex of ribozymes. (A) The catalytic triplex of the ribosome as seen in *C. reinhardtii*, with a table of all-atom RMSD values for each nucleotide of the triplex in other cryo-EM structures from bacteria and eukaryotes. Planar base triples are color-coded for clarity. (B) Comparison of the catalytic triplex present in group I and group II introns and the spliceosome.

Figure 1

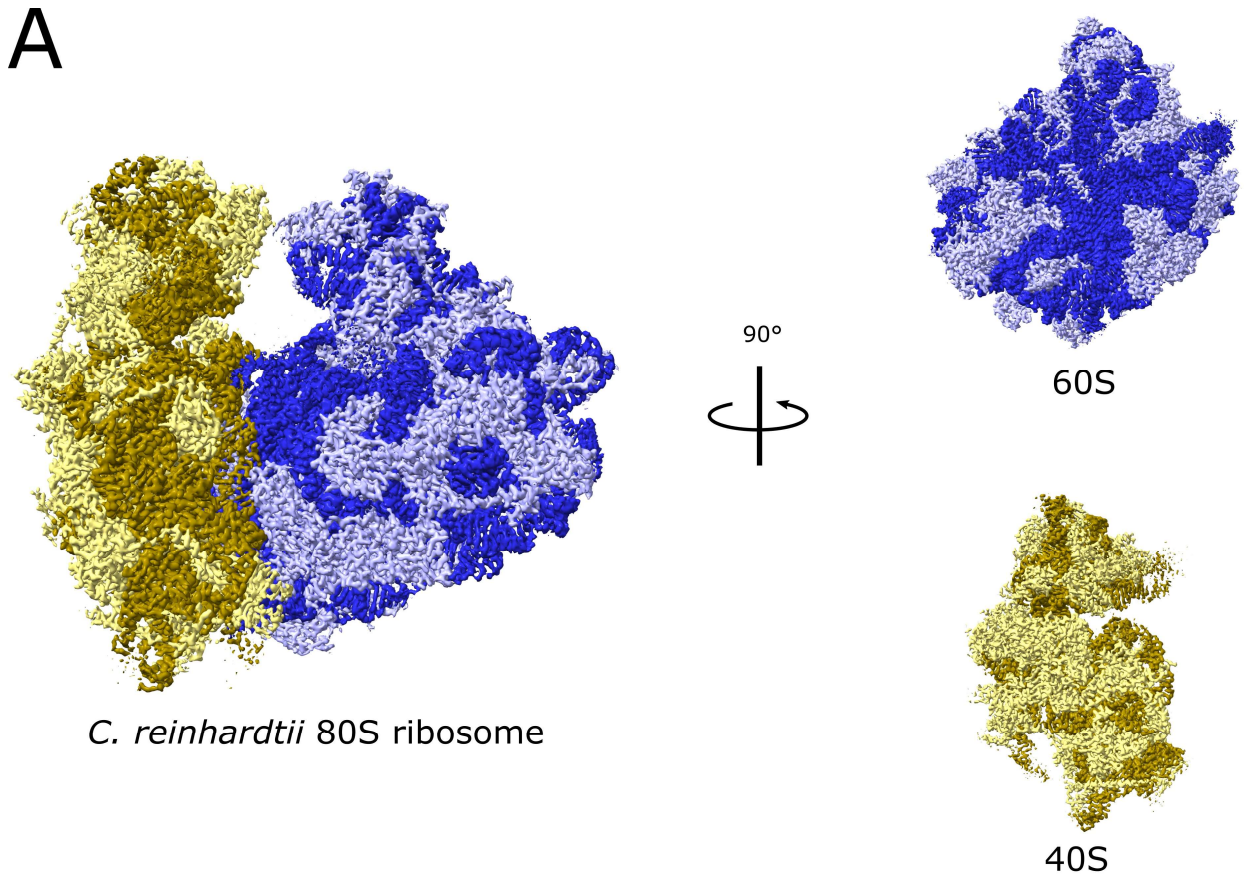
A
90°
60S
40S
C. reinhardtii 80S ribosome

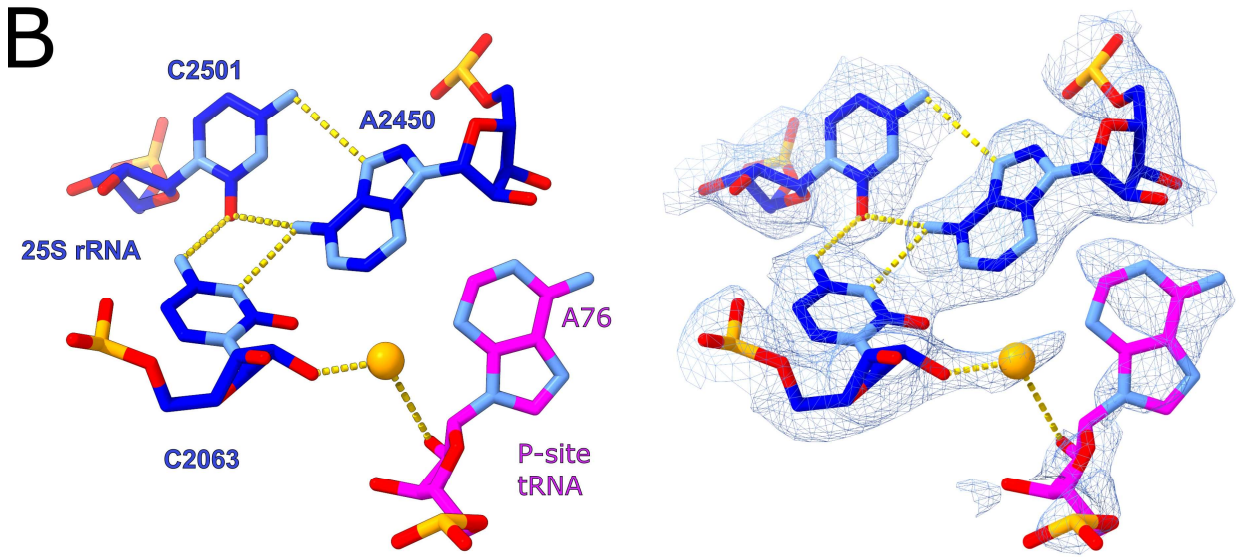
B
C2501
A2450
25S rRNA
A76
C2063
P-site
tRNA

Figure 2

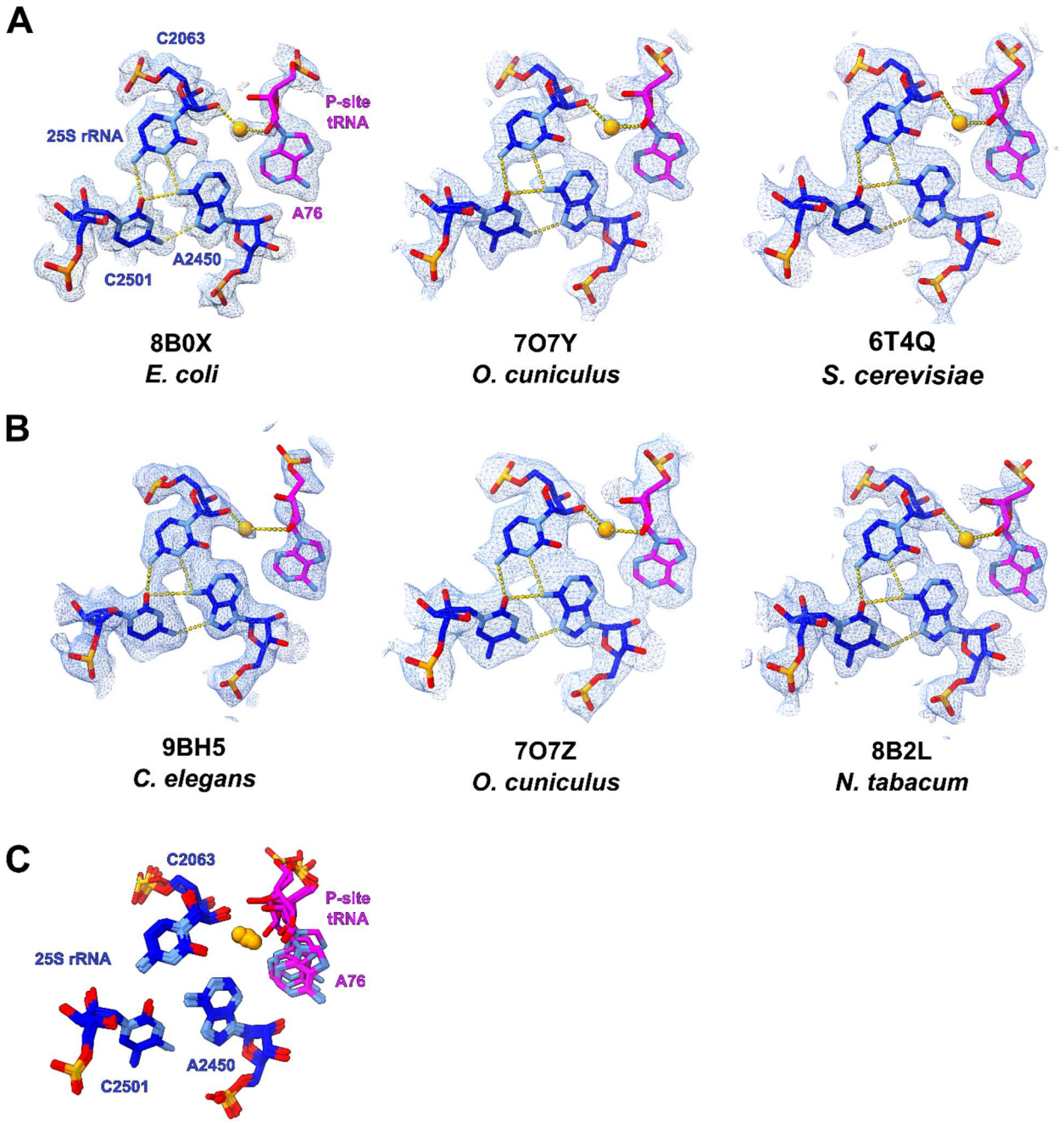
A
C2063
P-site
tRNA
25S rRNA
A76
A2450
C2501
8B0X
E. coli
7O7Y
O. cuniculus
6T4Q
S. cerevisiae
B
9BH5
C. elegans
7O7Z
O. cuniculus
8B2L
N. tabacum
C
C2063
P-site
tRNA
25S rRNA
A76
A2450
C2501

Figure 3

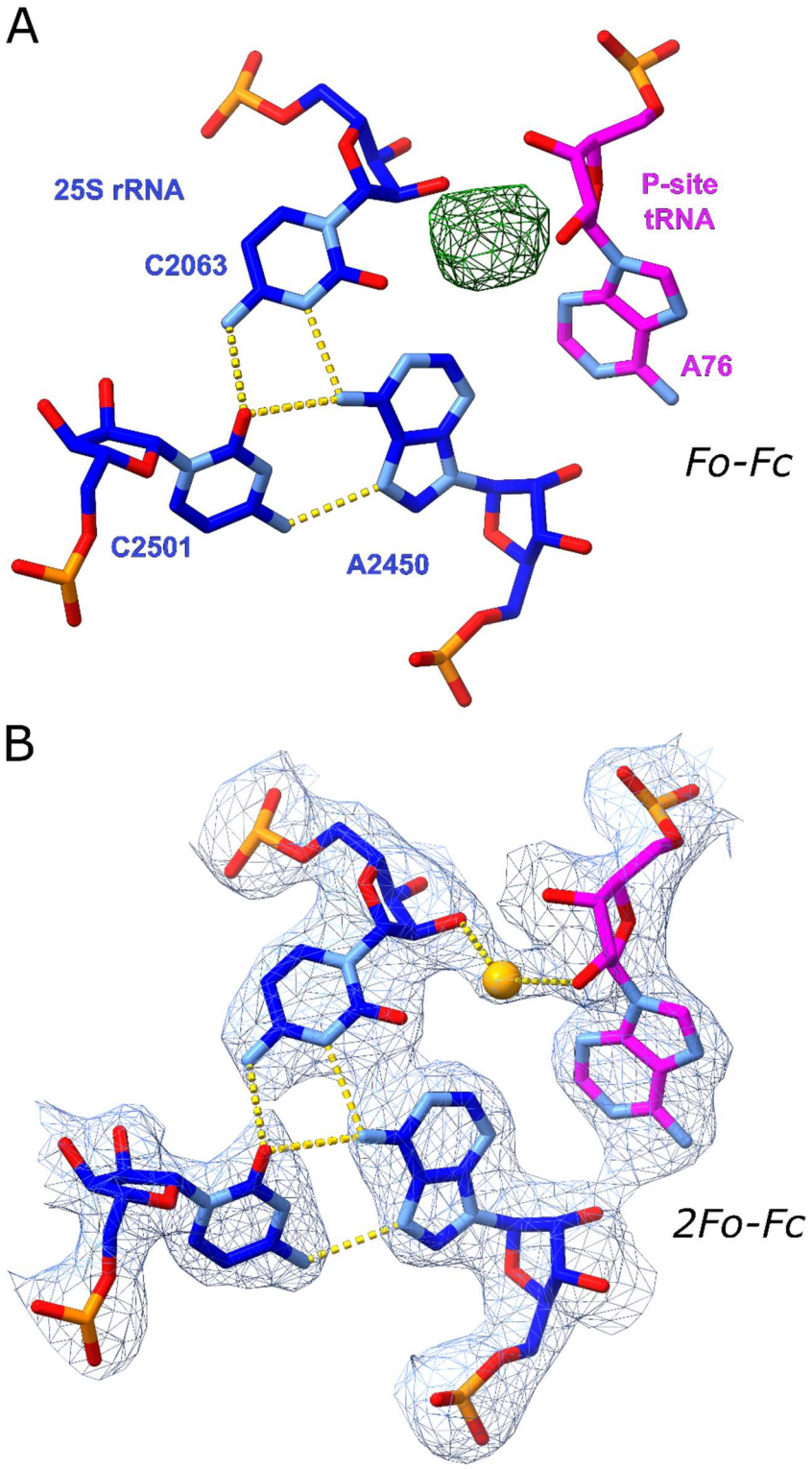

Figure 4

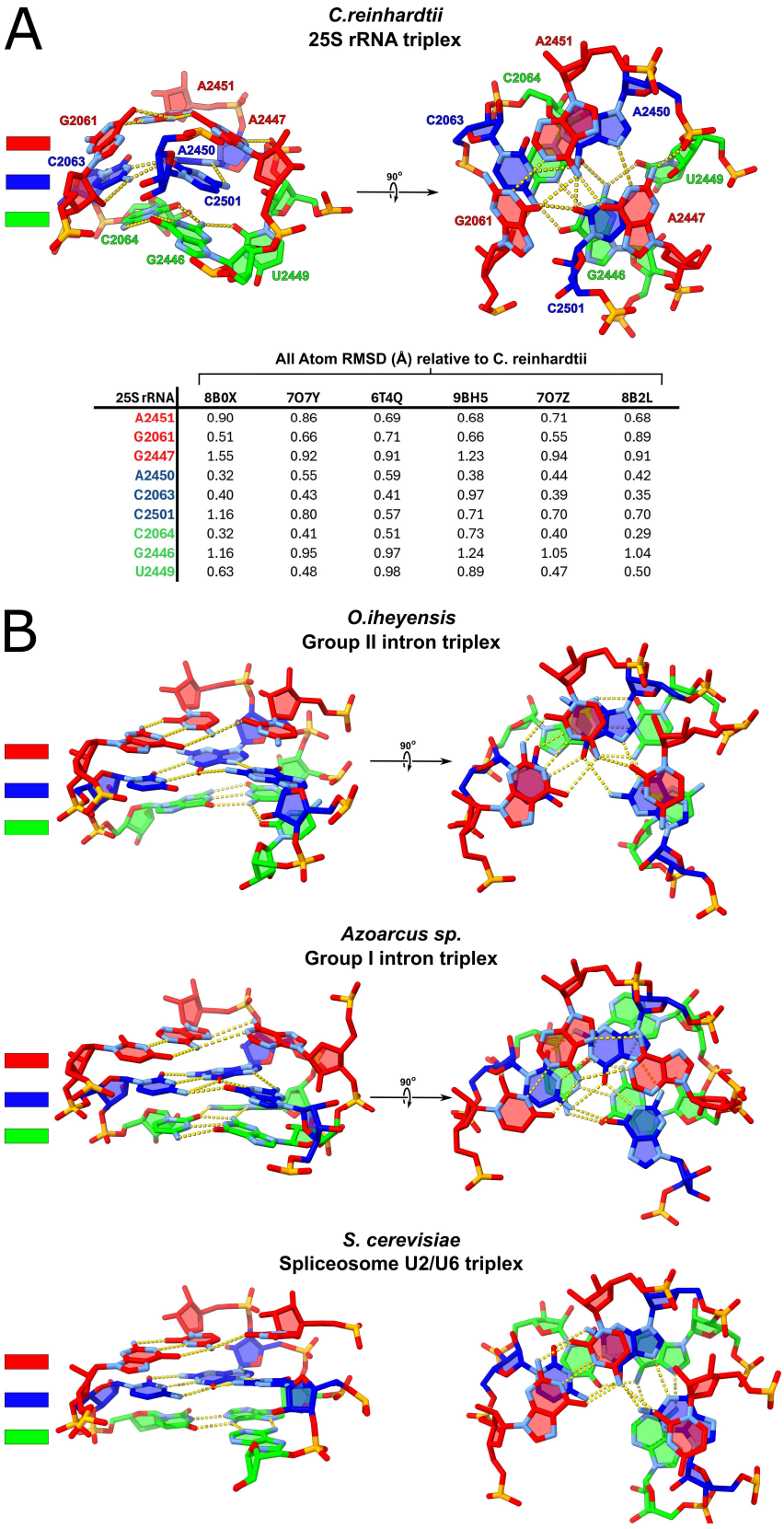

All Atom RMSD (Å) relative to C. reinhardtii

25S rRNA	8B0X	7O7Y	6T4Q	9BH5	7O7Z	8B2L
A2451	0.90	0.86	0.69	0.68	0.71	0.68
G2061	0.51	0.66	0.71	0.66	0.55	0.89
G2447	1.55	0.92	0.91	1.23	0.94	0.91
A2450	0.32	0.55	0.59	0.38	0.44	0.42
C2063	0.40	0.43	0.41	0.97	0.39	0.35
C2501	1.16	0.80	0.57	0.71	0.70	0.70
C2064	0.32	0.41	0.51	0.73	0.40	0.29
G2446	1.16	0.95	0.97	1.24	1.05	1.04
U2449	0.63	0.48	0.98	0.89	0.47	0.50